## Steady-state thermal characteristics of AMR read/write heads used in tape storage drives

I. E. T. Iben Y.-M. Lee W. D. Hsiao

Tape storage drives use lithographically deposited anisotropic magnetoresistive (AMR) sensors to read magnetic transitions written on tape. The read-back signal and the reliability of an AMR sensor are both affected by sensor temperature. Because current passes through the sensor, it is subject to joule heating, dependent on both the geometry of the sensor and the thermal conductivities of its material. Because of the resources required to build new sensors, the ability to predict the effects of dimensional changes on sensor temperature is important. This paper describes an analytical model and a three-dimensional finite element analysis (FEA) of the heat transfer for a shielded rectangular-sheet AMR sensor under joule heating over a range of sensor dimensions. The novel analysis consolidates the experimental and FEA data into a few parameters that make it possible to calculate the sensor temperature as a function of power for a wide range of geometries, thus assisting designers who need to set current limitations on the read elements of extant drives and to extrapolate to next-generation drives. We also evaluate the temperature of a sensor and the substrate in a drive, combining the heating from writers and readers. Heat flow away from the head substrate was found to be significantly higher when the tape is moving than when it is stationary, and a simple model is developed to describe the heat dissipation of the substrate as a function of tape velocity.

#### Introduction

Magnetic tape storage drives primarily use shielded anisotropic magnetoresistive (AMR) sensors to read signals written on magnetic tape [1–3]. The active portion of the sensors is deposited as thin rectangular resistive sheets (stripe) containing an AMR material. The resistance of an AMR material is greater when current is parallel to the magnetization direction than when the two vectors are perpendicular. Magnetic flux from the tape surface causes the sensor magnetization vector to rotate.

Electrical leads are used to connect to external devices. Current is passed through the sensor, and the AMR signal is measured as a voltage change. Current applied to the sensor also results in heating. With increasing temperature, the AMR effect decreases by approximately 0.01% °C<sup>-1</sup>, resulting in a decreased signal [4]. With increasing temperature, the AMR stripe and the shields can undergo magnetic changes [5–9] that can degrade the performance of the sensor. At higher temperatures and currents, diffusion or melting of the materials can cause

©Copyright 2003 by International Business Machines Corporation. Copying in printed form for private use is permitted without payment of royalty provided that (1) each reproduction is done without alteration and (2) the *Journal* reference and IBM copyright notice are included on the first page. The title and abstract, but no other portions, of this paper may be copied or distributed royalty free without further permission by computer-based and other information-service systems. Permission to *republish* any other portion of this paper must be obtained from the Editor.

0018-8646/03/\$5.00 © 2003 IBM

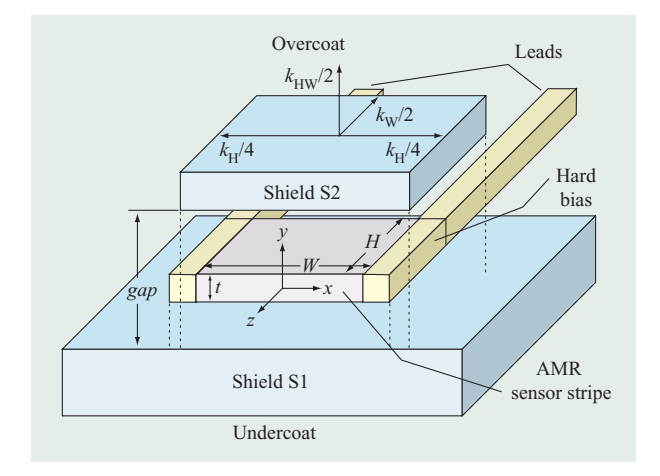


Figure 1

Schematic of the read-sensor layout.

degradation or destruction of the sensors [4, 6, 10–12]. Because of the close physical proximity of the shields to the stripe, shield temperatures rise as a result of thermal diffusion from a powered sensor. Elevated temperatures increase the rate of shield oxidation [6], which causes signal losses due to Wallace spacing [13]. Because tape heads use multiple sensors and writers embedded within a single substrate, the joule-heating power from the elements causes a rise in the substrate temperature [4]. Tapes are composed of plastic substrates with organic binders whose stability and glass transition temperatures are of the order of 40°C to 50°C [14]. Elevated temperatures of materials in the tape-head substrate can potentially accelerate physiochemical reactions and cause problems such as tape deterioration or head damage. To optimize performance and reliability, it is important to limit the temperature of the AMR sensor, the shields, and the substrate in which the sensors are embedded.

The temperature rise of a device is measured experimentally by the increase in the device resistance [4, 15, 16]. To determine the thermal distribution throughout a device as a function of geometry, both analytical [4, 17, 18] and finite element analysis (FEA) have been used [15, 19]. While analytical models of the thermal distribution in the sensor and the shields are useful, accurate models can be excessively complicated. Performing FEA computations is relatively standard with today's computers, but determining the appropriate parameters and comparing the results with experimental data can be difficult. To determine the stripe temperature as a function of current in a drive operation, it is preferable to be able to use a simple expression, rather than maintaining a multitude of plots for different sensor (stripe and shield) geometries and power levels. Considering the range of geometric

dimensions of tape-head readers, the need for a simple equation that predicts sensor temperature as a function of power becomes especially evident.

Figure 1 shows a schematic of the relevant components of a shielded AMR sensor. In the center of the figure is the AMR stripe, which, for thermal analysis, is a thinsheet resistor. The sheet lies in the xz plane. The readtrack width, W, lies along the x-axis, centered at x = 0, and the stripe height, H, points in the -z direction. The air-bearing surface (ABS) is in the xy plane at z = 0, with the tape surface just above z = 0. Tape passes along the ABS in the  $\pm v$  direction. The AMR sensor is separated from magnetically soft shields S1 and S2 by alumina, with the shield-to-shield spacing labeled gap. The shields are embedded in a solid undercoat and overcoat. The undercoat is then deposited onto a substrate, which is usually a hard ceramic material. Traditionally, an additional material, closure, is bonded onto the overcoat to protect the soft alumina and sensor materials from wear. Both the underlying substrate and the closure are referred to hereafter as the substrate. To form a functional tape head, the ABS is lapped (polished) to a highly smooth surface. This polishing decreases the value of H. The choice of the value of H (which can range over a factor of 2 or more) is based upon both performance [2, 3] and manufacturing tolerances. As the linear (y-axis) and transverse (x-axis) densities of magnetic transitions written to the tape are increased for higher storage capacity, gap, H, and W will decrease.

Data is written on tape in multiple parallel tracks along the length of the tape. To align the read sensors or writers with the desired tracks, special AMR sensors, termed servos, are located on the tape head to read pre-written data (servo patterns) from the tape. The servo information is then used to guide transverse motion of the head during reading or writing processes. The dimensions of the servos are usually different from those of the readers, with values of the order of one-half to two times the reader track width. Thus, within a product, the range of both H and W can vary greatly, so a simple analytical expression for evaluating the temperature of a stripe as a function of power and dimensions is extremely useful.

In this paper, we present simple analytical expressions to predict—as a function of the power applied to the AMR sensors and writers and of the tape velocity—the temperature of the sensors and the tape-head substrate when operating in a drive. The models to describe the joule heating of the sensors include the temperature dependence of the sensor sheet resistance and the dimensions of the sensor. The necessary parameters for the models are determined from experimental data. The average temperature of shielded AMR sheet resistors was measured as a function of both the current and the geometrical dimensions of the sensors. Steady-state FEA,

which includes the temperature dependence of the sheet resistance and the power deposition into the stripe, was performed to determine the distribution of temperatures throughout the entire reader, including the sheet resistor and surrounding shields. The initial values of the thermal properties of the materials were taken from literature and were adjusted to best fit the experimental data over a range of sensor dimensions. A simple analytical model is also developed to determine the tape-head substrate temperature as a function of power into the head from the readers and writers and the heat dissipation to moving tape. The models are then extended to operation in a drive.

## **Experimental details and results**

#### Materials

The AMR stripes used in this study were thin multilayered rectangular sheets that include an 81 Permalloy (81:19 Ni:Fe) sensor with self-biasing from a soft adjacent layer (SAL). Permanent magnets (hard bias) are located at the ends of the sheet resistors for further sensor biasing of the sensor magnetization. Figure 1 shows a schematic of the relevant components of the shielded AMR sensor, described above. The bulk of the data was collected on sensors with a gap of 0.37  $\mu$ m, a sensor Permalloy thickness ( $t_{mr}$ ) of 30 nm, a SAL thickness  $(t_{SAL})$  of 24 nm, and a sheet resistance  $(R_{\text{sheet}})$  of 6.2  $\Omega/\square$ . Some parts were studied that had a gap of 0.5  $\mu$ m, a  $t_{\rm mr}$  of 40 nm with a  $t_{\rm SAL}$  of 32 nm, and an  $R_{\rm sheet}$  of 4.6  $\Omega/\Box$ . S1 is 1.8- $\mu$ m-thick annealed Sendust (Fe:Si:Al, 83:12:5). S2 is 3-\mum-thick 81 Permalloy. The sensor stripes have read-track widths (W) between 4  $\mu$ m and 13  $\mu$ m and read-stripe heights (H) that range from 1.4  $\mu$ m to 3.4  $\mu$ m.

While older tape products used magnetic nonconductive ferrite substrates on which the sensors were deposited [4, 14], the substrate used in this study was made of nonmagnetic conductive AlTiC. Furthermore, while conventional tape heads use a contoured ABS [14], the tape head we studied has a flat-lapped ABS [20]. The area of the ABS in contact with tape is 4.8 mm<sup>2</sup>.

The tape used has four layers: a 0.2- $\mu$ m thick magnetic layer of  $\gamma Fe_2O_3$  magnetic particulates and a binder; a 2- $\mu$ m-thick underlayer of nonmagnetic metal-oxide particulates embedded in a binder; a 6- $\mu$ m-thick polyethylene naphthalate (PEN) layer; and a 0.5- $\mu$ m-thick back coat. The density, heat capacity, and thermal conductivity of the magnetic layer are approximately  $1.7~{\rm g~cm^{-3}}$ ,  $1~{\rm J~g^{-1}~^{\circ}C^{-1}}$ , and  $0.41~{\rm W~m^{-1}~^{\circ}C^{-1}}$ , respectively [14]. The underlayer should have properties similar to those of the magnetic layer. The density, heat capacity, and thermal conductivity of the base layer are approximately  $1.3~{\rm g~cm^{-3}}$ ,  $1.27~{\rm J~g^{-1}~^{\circ}C^{-1}}$ , and

0.19 W m<sup>-1</sup> °C<sup>-1</sup>, respectively<sup>1</sup> [21]. To ensure close contact of the ABS and the tape surface, tape moving over the surface overwraps the leading and trailing edges of the substrate.

# Sensor resistance as a function of stripe dimensions and temperature

The sensor resistance  $(R_{\rm total})$  is a series combination of the resistance of the leads, the hard bias  $(R_{\rm lead-hb})$ , and the active AMR stripe section  $(R_{\rm mr})$ . For a device, the track width is fixed to high accuracy in the wafer lithography process and its value is known. Owing to lapping tolerances in the preparation of the sensor, the stripe height varies from one sensor to another, and its value must be calculated from the total measured resistance using the equations

$$R_{\rm mr}(T_{\rm mr}) = [W/H]R_{\rm sheet}(T_{\rm mr}) = R_{\rm total}(T_{\rm mr}) - R_{\rm lead\text{-}hb} \tag{1a}$$

an

$$H = W(R_{\text{sheet}})(T_{\text{mr}})/[R_{\text{total}}(T_{\text{mr}}) - R_{\text{lead-hh}}]. \tag{1b}$$

The stripe sheet resistance  $(R_{\rm sheet})$  is a function of the stripe temperature  $(T_{\rm mr})$ . The combined resistance of the lead and hard bias  $(R_{\rm lead-hb})$  is  $7.5\pm0.7~\Omega$  for the parts. Although the stripe comprises multiple layers, it is very thin and is treated as a single sheet with an effective homogeneous sheet resistance. To determine the temperature of an AMR stripe, it is necessary to know  $\alpha_{\rm mr}$ , the thermal coefficient of fractional resistance change per temperature change of the AMR stripe, as defined by

$$R_{\rm mr}(T_{\rm mr}) = R_{\rm mr}(T_{\rm st})[1 + \alpha_{\rm mr}(T_{\rm mr} - T_{\rm st})], \tag{2}$$

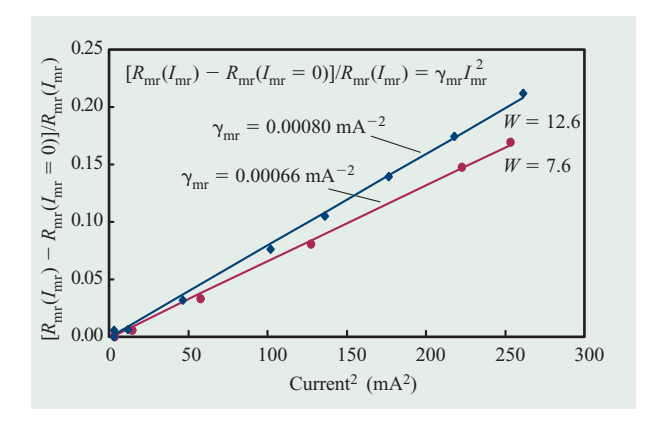
where  $T_{\rm st}$  is an arbitrarily chosen standard temperature (= 25°C). To determine  $\alpha_{\rm mr}$  experimentally, the leads of an AMR sensor are bonded to a cable, and the cabled sensor is heated in an oven while the resistance is measured as a function of temperature. For an accurate determination of  $\alpha_{\rm mr}$ , the temperature-dependent resistances of the leads and the cable are measured and subtracted from the total measured resistance. The quantity  $\alpha_{\rm mr}$  is determined to be  $0.0025 \pm 0.0001^{\circ}{\rm C}^{-1}$ .

## Joule heating and thermal conductance

A simple empirical model for predicting the temperature rise of an AMR stripe as a function of current is to assume that the joule-heating temperature rise of the sensor ( $\Delta T_{\rm mr-joule}$ ) is proportional to the power deposited in the stripe ( $P_{\rm mr}$ ), as given by

$$\Delta T_{\text{mr-joule}} = P_{\text{mr}}/k_{\text{mr}} = R_{\text{mr}}(T_{\text{mr}})I_{\text{mr}}^2/k_{\text{mr}}, \qquad (3)$$

<sup>1</sup> Values are for polyethylene terephthalate, a common base used for magnetic storage tapes.



Data and fit for transformed AMR stripe resistance as a function of current squared for sensors with a  $t_{\rm mr}$  of 30 nm, an H of 2.2  $\mu$ m, a gap of 0.37  $\mu$ m, and a W of 7.6 and 12.6  $\mu$ m.

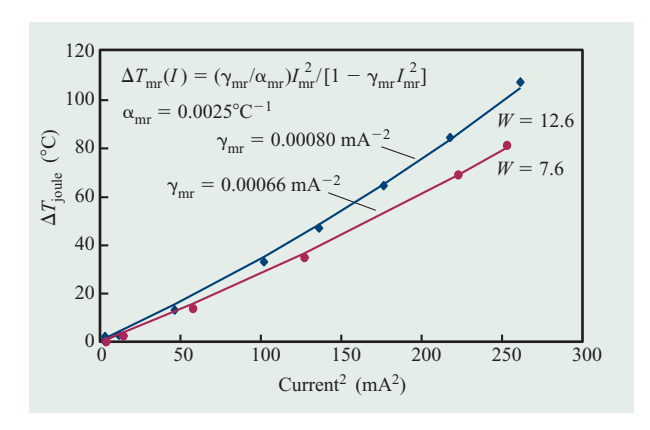


## Figure 3

Data and fit for the AMR stripe joule-heating temperature as a function of current squared for the same parts shown in Figure 2.

where  $I_{\text{mr}}$  is the current passing through the sensor and  $k_{\text{mr}}$  is the AMR sensor thermal conductance.

Combining Equations (2) and (3) yields the AMR resistance and joule-heating temperature rise as functions of current, as shown respectively in Equations (4a) and (4b):

$$R_{\rm mr}(I_{\rm mr}) = R_{\rm mr}(I_{\rm mr} = 0)/[1 - \gamma_{\rm mr}I_{\rm mr}^2]$$
 (4a)

and

$$\Delta T_{\text{mr-joule}} = (\gamma_{\text{mr}}/\alpha_{\text{mr}})I_{\text{mr}}^2/[1 - \gamma_{\text{mr}}I_{\text{mr}}^2], \tag{4b}$$

with  $\gamma_{mr}$  defined through

$$k_{\rm mr} = \alpha_{\rm mr} R_{\rm mr} (I_{\rm mr} = 0)/\gamma_{\rm mr} \,. \tag{4c} \label{eq:kmr}$$

The physically relevant parameter  $k_{\rm mr}$  is derived from the resistance versus current data using the fitting parameter  $\gamma_{\rm mr}$ 

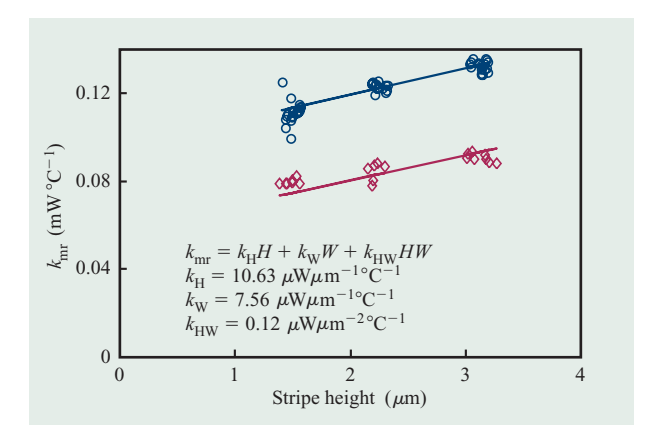


## Figure 4

Thermal conductance as a function of stripe height of AMR sensors with a  $t_{\rm mr}$  of 30 nm, a gap of 0.37  $\mu$ m, and track widths of 7.6  $\mu$ m (red diamonds) and 12.6  $\mu$ m (blue circles).

[Equation (4c)]. To extract  $\gamma_{mr}$ , Equation (4a) can be rearranged to give a function that is linearly dependent on the square of the sensor current:

$$[R_{\rm mr}(I_{\rm mr}) - R(I_{\rm mr} = 0)]/R_{\rm mr}(I_{\rm mr}) = \gamma_{\rm mr}I_{\rm mr}^2.$$
 (5)

Figure 2 is a plot of the transformed AMR resistance given in Equation (5) as a function of current squared for two AMR stripes with two different track widths of 7.6 and 12.6 µm, with other geometrical values remaining the same. The  $t_{mr}$  was 30 nm, and the gap and stripe height were 0.37  $\mu$ m and 2.2  $\mu$ m, respectively. Figure 3 shows the experimentally determined and calculated joule-heating temperature rise plotted against current squared for the same AMR sensors shown in Figure 2. The experimentally determined temperature rise is derived from the measured resistance using Equation (2) with Equations (1a) and (1b). The calculated temperature rise uses Equation (4b) with the experimentally determined  $\gamma_{mr}$  of Figure 2. Note that for the same current or current density, the sensor (servo) with  $W = 7.6 \mu m$  is cooler than the sensor (reader) with  $W = 12.6 \mu m$ .

## Experimental model for thermal conductance

Thermal conductance varies with sensor geometry. Thus, to predict the temperature of AMR stripes as a function of bias current for a range of geometries, we measure the thermal conductance for a range of stripe heights and track widths. **Figure 4** is a plot of the experimentally determined thermal conductance as a function of stripe height for AMR sensors with track widths of 12.6 and 7.6  $\mu$ m, which are lapped to stripe heights between 1.4 and 3.4  $\mu$ m. For a fixed gap, the stripe height and track

**Table 1** Thermal conductance parameters from FEA and experiments.

Туре	W range (μm)	H range (μm)	Gap (μm)	$(W \circ C^{-1} m^{-1})$	$(\mathbf{W} \circ \mathbf{C}^{-1} \mathbf{m}^{-1})$	$k_{ m WH}  imes 10^6 \ ( m W  ^{\circ}  m C^{^{-1}}  m^{^{-2}})$
FEA	4-13	1-4	0.37	$10.4 \pm 2.1$	$6.0 \pm 0.6$	$0.86 \pm 0.22$
Wafer 1, line 1*	7.6 - 12.6	1.5-3.5	0.37	$11.3 \pm 4.4$	$7.5 \pm 0.9$	$0.06 \pm 0.4$
Wafer 2, line 2*	7.6 - 12.6	1.5-3.5	0.37	$9.2 \pm 0.9$	$7.7 \pm 0.2$	$0.33 \pm 0.09$
Wafer 3, line 2*	4-12.6	2-4	0.37	$7.0 \pm 1.5$	$8.8 \pm 0.9$	$0 \pm 0.3$
Wafer 4, line 2*	4-12.6	2-4	0.5	$6.0 \pm 1.5$	$7.5 \pm 0.9$	$0 \pm 0.3$

<sup>\*</sup>Lines 1 and 2 are distinct deposition locations and tools.

width dependence of the thermal conductance is modeled by the empirical second-order quadratic equation,

$$k_{\rm mr} = k_{\rm H}H + k_{\rm W}W + k_{\rm HW}HW, \tag{6}$$

where  $k_{\rm H}$ ,  $k_{\rm W}$ , and  $k_{\rm HW}$  are dependent on the thermal conductivities and dimensions of the gap, shields, and overcoat.

Also shown in Figure 4 are the best  $\chi$ -square minimization fits using the parameters  $k_{\rm H}$ ,  $k_{\rm W}$ , and  $k_{\rm HW}$ , whose values are tabulated in **Table 1** (wafer 1). Values of the thermal-conductance-fitting parameters derived from experiments using wafers with different sensor geometries or different deposition tools are also given in Table 1. The errors in the fitting parameters are one standard deviation in the mean-square deviation between the fit and the data.

In addition to being dependent on stripe height and track width, the thermal conductance parameters are also gap-dependent. Values of thermal-conductance-fitting parameters as a function of stripe height and track width for a gap of 0.5  $\mu$ m are given in Table 1 (wafer 4, line 2). The fact that thermal conductance decreases with increasing gap emphasizes the importance of including the shields in an analysis of the heat flow. Wafers 3 and 4 are used to compare the effect of the gap on the thermal conductance, because all other parameters are identical for these parts, and the wafers are deposited using the same tools in the same physical location. The ratio of the measured thermal conductance at a gap of 0.50  $\mu m$ compared with a gap of 0.37  $\mu$ m  $(k_{0.50}/k_{0.37})$  was 0.85  $\pm$  0.01 for track widths of 4 and 12.6  $\mu m$  and stripe heights between 2 and 4  $\mu$ m (wafers 3 and 4). Given the size of the gaps compared with the surrounding material, the shields act as heat sinks, drawing away much of the heat from the AMR stripe. If the temperature drop to ambient temperature occurred entirely across the gap,  $k_{mr}$  would vary inversely with the gap, and  $k_{\rm 0.50}/k_{\rm 0.37}$  would be expected to be 0.74. A more accurate representation of the dependence of  $k_{mr}$  on gap is  $\sqrt{1/gap}$ . Equation (6) can then be modified to include the gap dependence of the thermal conductance:

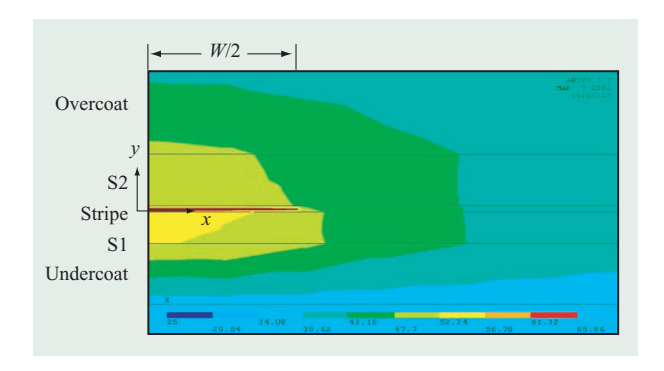
$$k_{\rm mr} = \sqrt{\frac{gap_0}{gap}} (k_{\rm H}H + k_{\rm W}W + k_{\rm HW}HW),$$
 (7)

where  $gap_0$  is arbitrarily chosen to be 0.37  $\mu$ m. With only two gaps studied, the dependence is not well substantiated. The value of  $k_{0.50}/k_{0.37}$  is between unity and the ratio of the gaps because the shields are not perfect heat sinks and are at a temperature intermediate between the stripe and the ambient value.

## Thermal modeling

The FEA was carried out using the commercial software tool ANSYS\*\*, with an approach similar to that described by Young [15]. Also, the mesh size was varied appropriately for the size and location of the material. The sensor, which was thin and was the source of the heat, had a fine mesh, as did the thin-gap alumina. The shields, which were close to the sensor, also had a fine mesh size, but larger than that of the sensor. Regions farther from the heat source had a coarser mesh size. The model also included the temperature-dependent electrical resistivity of the sensor in the calculations. The boundary conditions set the temperature of the substrate and closure at 25°C.

The thermal conductivity parameters used in the FEA are taken from the literature and adjusted to best fit the experimental data over a range of sensor geometries. The thermal conductivity of the AlTiC substrate was taken to be 20 W m<sup>-1</sup> °C<sup>-1</sup>. Owing to the relative thickness of the shields, the thermal conductivities of S1 and S2 should be similar to their bulk values and related to their electrical conductivity [19]. The electrical resistivity of Sendust and Permalloy 81 are around 80  $\mu\Omega$ -cm and 15  $\mu\Omega$ -cm, respectively [11]. Correlation with allows listed in the CRC Handbook of Chemistry and Physics [22] indicates that the thermal conductivities of Sendust and Permalloy should be in the range of 13 to 20 W m<sup>-1</sup> °C<sup>-1</sup> and 40 to 60 W m<sup>-1</sup> °C<sup>-1</sup>, respectively, which are higher values than those used in this report. The thermal conductivities used for the metals were 120, 8.5, and 21 W m<sup>-1</sup> °C<sup>-1</sup> for the leads, shield S1, and shield S2, respectively. The values of S1 and S2 are similar to those reported in other FEAs:



Temperature distribution in the neighborhood of an AMR stripe on the air-bearing surface. The temperature along the track is quite uniform, and the highest temperature occurs in the middle of the AMR stripe, as expected. The maximum temperature rise is about 41°C.

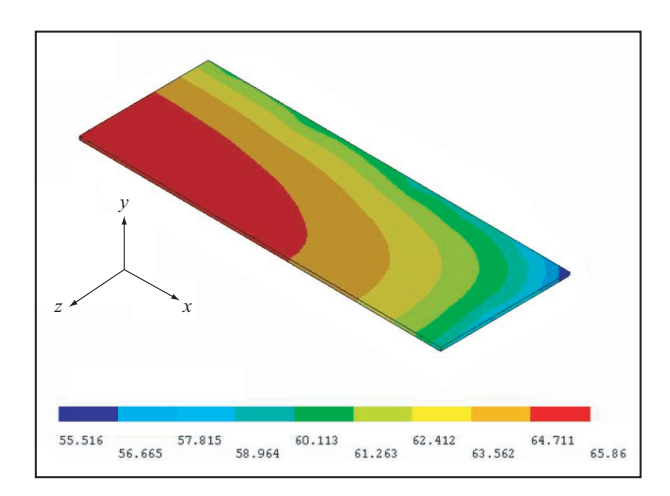


#### Figure 6

Temperature distribution of an AMR sensor. Because of symmetry, only half of the AMR stripe is shown.

9 and 40 W m<sup>-1</sup> °C<sup>-1</sup> in [19], and a single value of 13 W m<sup>-1</sup> °C<sup>-1</sup> in [15]. While the thermal conductivity of the thick overcoat and undercoat aluminas might be close to the bulk values, the thermal conductivity of the thin-gap alumina is very different from the bulk values [19, 23]. The optimum thermal conductivity for the gap alumina was 1.5 W m<sup>-1</sup> °C<sup>-1</sup>, which is intermediate between the values of 1 and 3.5 W m<sup>-1</sup> °C<sup>-1</sup> reported by Ju et al. and Young [15, 19].

An isothermal contour plot at the ABS is shown in **Figure 5**, using a power in the sensor of 5.2 mW for a stripe with a  $t_{\rm mr}$  of 30 nm and a track width, stripe height, and gap of 12.6, 2.25, and 0.37  $\mu$ m, respectively. As

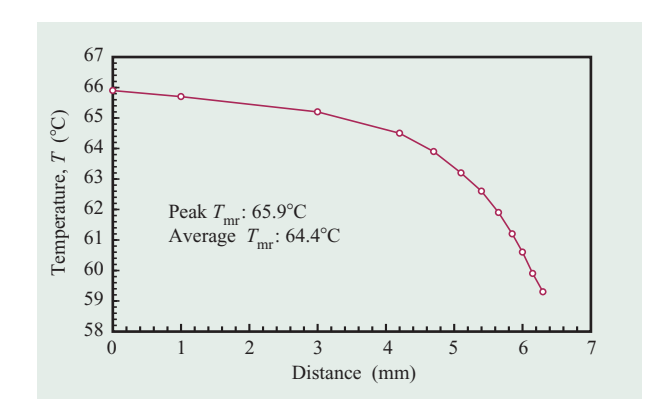


## Figure 7

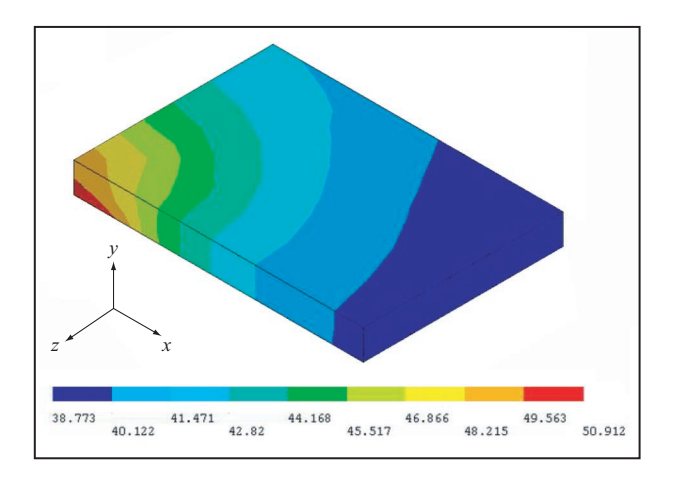
Temperature distribution of the AMR stripe along the track width on the air bearing surface from the center to the track-width edge.

expected, the AMR stripe is the hottest region. The shields are also at elevated temperatures, with the fractional joule-heating temperatures of the shields within the width of the stripe being over 75% of the average sensor temperature rise. Furthermore, shield S2, which is thinner and has the lower thermal conductivity, is hotter than shield S1.

An isothermal contour plot of the sensor is shown in Figure 6. The thermal distribution within the sensor is relatively uniform, as seen in Figure 7, which is a plot of the temperature of the AMR stripe along the ABS from the center of the stripe to the track-width edge. The temperature of the shields is also important. Figure 8 shows an isothermal temperature distribution of shield S2, using a power in the sensor of 5.2 mW. The precipitous temperature drop from the stripe to the shield is evidence of the large effect on the thermal distribution from the relatively high thermal conductivity of the shield compared with that of the gap or overcoat alumina. The ratio of the maximum joule-heating temperature rise of shield S2 (26°C) compared with that of the stripe (41°C) is 63%, with the drop occurring over a distance of  $\sim 0.16 \mu m$ . The remaining drop in heat through the overcoat alumina occurs over a distance of  $\sim$ 25  $\mu$ m. The fact that the shields serve as major heat sinks for the sensor is shown experimentally by the dramatic dependence of the sensor thermal conductance on the gap size.

## Comparison of experiments with FEA and other models

The thermal conductance as a function of stripe height and track width is used to compare the temperatures determined by FEA with the experimental values. The thermal conductance measured by FEA is calculated by dividing the deposited power by the average AMR



Temperature distribution of the shield S2. Because of symmetry, only half of the shield is shown. The highest temperature occurs at the region near the AMR stripe and approaches the AMR average temperature.

temperature. FEA calculations of sensor temperature rise using a constant current density and a temperatureindependent sheet resistance and including the effects of leads for a range of track widths and stripe heights for a gap of 0.37  $\mu$ m are tabulated in **Table 2** and plotted in Figure 9. The thermal conductivities given earlier have been adjusted to give a best fit to the experimentally determined values of thermal conductance, as shown in Figure 9. Also shown in the figure is the fit to the FEA thermal conductance using Equation (6), and the results are given in Table 1 (FEA). The FEA and the experimental values agree within several percent over the range of stripe heights and track widths measured. The differences are due to a combination of experimental errors and approximations used for both the FEA and the experimental analysis. FEA calculations without lead leakage yield similar results, but they do not yield as good a fit for the full range of stripe heights and track widths studied as when the lead leakage is included.

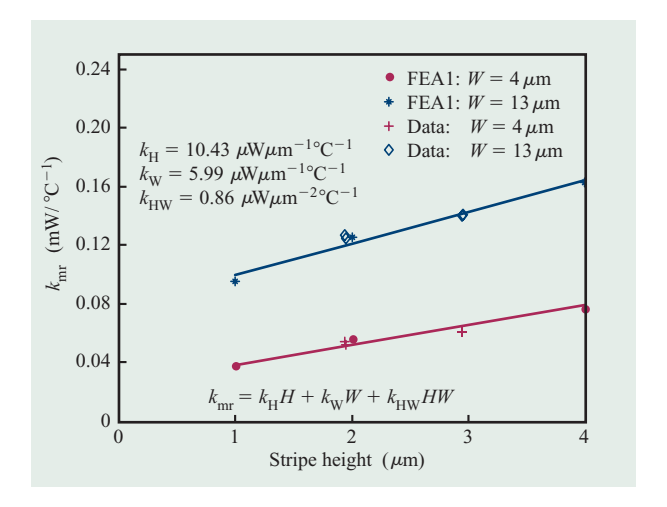


## Figure 9

Data and FEA calculations. Conductivities used for the FEA adjusted to give the best fit to the data; the fit to  $k_{\rm mr}$  is the best fit to the FEA data.  $R_{\rm sheet}$  is  $4.62~\Omega/\Box$  and the gap is  $0.37~\mu{\rm m}$ .

#### Interpretation of thermal conductance parameters

The quantity  $k_{\rm mr}$  contains the thermal conductivities of the leads, gap, overcoat alumina, and shields, as well as the sensor dimensions. Under certain assumptions, the thermal conductance can be calculated analytically. For example, assuming that the shields are perfect heat sinks (no temperature rise above ambient) and W is large, Guo and Ju [18] obtain the equivalent of Equation (4b) [see their equation (7)] if one chooses  $k_{\rm mr} = 2(k_{\rm Al}/gap)HW$ , where  $k_{\rm Al}$  is the thermal conductivity of the gap alumina. However, the data and FEA presented in Equation (7) of the present paper reach a quite different conclusion. Because the shields are not perfect heat sinks, the geometric dependence of the thermal conductance is very different from the simple analytical expression.

An instructive way of understanding the thermal conductance parameters is to examine the relative contributions made by the three thermal conductance

**Table 2** Average joule-heating temperature rise,  $\langle \Delta T_{\text{joule}} \rangle$ , from FEA at a constant current density. The AMR gap was 0.37  $\mu$ m, and  $R_{\text{sheet}}$  was 4.62  $\Omega/\Box$ . The AMR resistance was held fixed. Heat flux from the leads was included in the model.

	Track width = $4 \mu m$			Track width = $13 \mu m$			
Stripe height (µm) Total current (mA) Power (mW)	1 15 4.16	2 30 8.32	4 60 16.63	1 15 13.51	2 30 27.03	4 60 54.05	
$<\Delta T_{\rm joule}>$ (°C)	94	126	186	122	185	285	
Thermal conductance ( $\mu W/^{\circ}C$ )	44	66	89	111	146	190	

**Table 3** Thermal conductance and fractional contributions to the heat flux from  $k_{\rm H}$ ,  $k_{\rm W}$ , and  $k_{\rm HW}$  for different W and H values using parameters from FEA and experiments.

Туре	gap		$W = 12.6 \ \mu m, \ H = 2.25 \ \mu m$				$W = 5.4 \mu m, H = 1.25 \mu m$			
	(µm)	$k_{\rm H}H$ $(\%)$	k <sub>w</sub> W (%)	k <sub>wH</sub> WH (%)	$k \pmod{\text{mW} \circ \text{C}^{-1}}$	$k_{\rm H}H$ $(\%)$	$k_{\mathrm{W}}W$ $(\%)$	k <sub>wH</sub> WH (%)	$(\text{mW}  {}^{\circ}\text{C}^{-1})$	
FEA	0.37	19	61	20	0.123	25	63	11	0.051	
Wafer 1, line 1*	0.37	21	78	1	0.122	26	74	1	0.055	
Wafer 2, line 2*	0.37	16	76	7	0.127	21	75	4	0.055	
Wafer 3, line 2*	0.37	12	88	0	0.127	16	84	0	0.056	
Wafer 4, line 2*	0.5	13	88	0	0.108	16	84	0	0.048	

<sup>\*</sup>Lines 1 and 2 are distinct deposition locations and tools.

parameters to the total thermal conductance, as shown in **Table 3.** For both the data and the FEA, the  $k_{HW}HW$ term, which is the dominant term if the shields are assumed to be perfect heat sinks, contributes the least amount of long-range heat flux. The dominant longrange heat flux is from the linear terms  $k_H H$  and  $k_W W$ . The linear terms are dominant not because of heat flow through the thin ends of the sensor sheet, but because of the three-dimensional nature of the heat flow through the media surrounding the sensor, particularly the shields. For the dimensions of extant tape heads, heat flow through the leads is minimal. Though the bulk of the heat leaves the sensor sheet through the sheet surface area, 2HW, it diffuses from the surrounding materials in three dimensions, causing the temperatures in close proximity to the sensor to fall more rapidly than would result from a one-dimensional model, where heat flow is only in the ±y direction. As seen in Figures 7 and 8, the temperature drops substantially (by about 37%) across the gap, but not to room temperature, as in the case of an infinite thermal conductivity for the shields [18]. The large temperature drop across the narrow gap (compared with the undercoat and overcoat alumina and metal shields) indicates that the dominant heat flow is through the highly conductive shields. The dominance of the linear terms  $k_{\rm w}W$  and  $k_{\rm H}H$ reflects the fact that the dominant flow of heat is in the xz plane of the shields (Figure 1). The heat flow to shields S1 and S2 is assumed to be identical. The  $k_wW$  term is associated with heat flow through the shields in the -z direction, while the  $k_{\rm H}H$  term is associated with heat flow in both the +x and -x directions. Heat flow through the leads also contributes to the  $k_{\rm H}H$  term. Thus, the magnitude of the  $k_{\rm H}$  term should be larger than that of the  $k_{\mathrm{W}}$  term as a result of two effects: 1) the heat flux through the leads; and 2) the fact that heat flow in the solid shields has two paths perpendicular to H, in both the +x and -x directions, and only one path perpendicular to W, in the -zdirection. The  $k_{\rm w}W$  term is much larger than the  $k_{\rm H}H$ term because  $W/H \gg 1$ .

An analytical expression to fit the temperature rise of AMR stripes with large W/H ratios (5.5 to 150) was used by Dee and Thornly [4],

$$k_{\text{mr-Dee}} = \frac{W}{A + B \log_{P}(W/H)},$$
 (8)

implying that the thermal conductance is dominated by heat flux in the material surrounding the sensor. Equation (8) does not include the effects of leads. While the data collected by Dee and Thornly requires that the parameters A and B be of opposite sign, the data reported here requires that the signs of both A and B be positive, indicating that although Equation (8) is useful, a direct physical interpretation of the parameters A and B is not evident. Furthermore, while the analytical expression used by Dee and Thornley can be used to summarize the data reported here, the second-order expression of Equation (6) is easier for understanding the effects of B and B0 on limiting the sensor currents in a drive.

## Extrapolation of the thermal conductance to smaller dimensions

Equation (7), which includes the dependence of the thermal conductance on W, H, and gap, can be used to extrapolate to smaller dimensions. Figure 10(a) is a plot of the average temperature rise as a function of the stripe height of a giant-magnetoresistive (GMR) sensor [19] that had a track width of 0.4  $\mu$ m, a value range for H of 0.2 to 0.6  $\mu$ m, and a gap of 30 nm, with an applied current of 5 mA. The GMR sensor, which was designed for use in high-density disk drives (HDDs), is also a shielded thin-sheet MR sensor with a structural design similar to that of the AMR sensor used in tape heads, but the multilayered sensor sheet is composed of different materials from those used in an AMR sensor, and the dimensions are significantly smaller.

**Figure 10(b)** is a plot of the thermal conductance as a function of stripe height of the same GMR sensor calculated from the data in Figure 10(a) using Equation (3) with

Equations (1) and (2). The values for  $R_{\rm sheet}$  and  $\alpha_{\rm mr}$  were taken as  $20~\Omega/\Box$  and  $0.001^{\circ}{\rm C}^{-1}$ , respectively. Also shown in Figure 10(a) is an extrapolation of the thermal conductance parameters used to fit the data in Figure 9 using Equation (7), which reduces to  $k_{\rm mr}=4.9+21.9H~\mu{\rm W}/^{\circ}{\rm C}$  (H is in  $\mu{\rm m}$ ) for the data. To achieve the fit shown in the figure, the extrapolated thermal conductance values were all decreased by a multiplicative scaling factor ( $f_{\rm scale}$ ) of 0.58. The other thermal conductance parameters given in Table 1 yield similar fits to the data shown in Figures 10(a) and 10(b) with scaling factors between 0.5 and 0.58. The extrapolated temperature rise as a function of stripe height was also calculated and is shown in Figure 10(a). Equations (4b) and (4c) and the extrapolation parameters shown in Figure 10(b) were used.

The fact that a scaling factor is necessary to accurately fit the thermal conductance for the HDD sensor using the parameters determined for the tape drive sensor is not surprising considering the fact that the gap, H, and W are each decreased by more than a factor of 10 for the GMR sensors compared with the AMR sensors. The relative shield sizes are also not identical. The fact that the extrapolation works so well over such a large range of dimensions is because the structures are similar in their overall design, both being thin rectangular sheets with metal shields. One reason for requiring a scaling factor (between 0.5 and 0.58) for the extrapolated thermal conductance could be that the thermal conductance of the gap alumina is thickness-dependent [19, 23] in the thickness range of 13-160 nm. Another possibility is that thermal leakage through the leads differs between designs and dimensions. Furthermore, the shield dimensions affect the sensor thermal conductance. Finally, the dependence of the thermal conductance on  $\sqrt{1/gap}$  has been established for only a narrow range of gaps and requires further study to validate its use over a wider range. The extrapolation was not given to advocate its use over such a wide range in sensor dimensions, but rather to lend support to the use of Equation (7) in making projections to futuregeneration tape-head sensors prior to their fabrication.

## Projected joule-heating temperature as a function of current

Thermal conductance can be used to calculate the temperature rise of an AMR stripe using Equation (4b). **Figure 11** shows the average joule-heating temperature rise as a function of current for a sensor with a  $t_{\rm mr}$  of 30 nm, a W of 13  $\mu$ m, and a gap of 0.37  $\mu$ m for four different stripe heights. As expected, for a fixed current, the shorter the stripe height, the greater the joule-heating temperature rise. What is not evident in Figure 11 is that

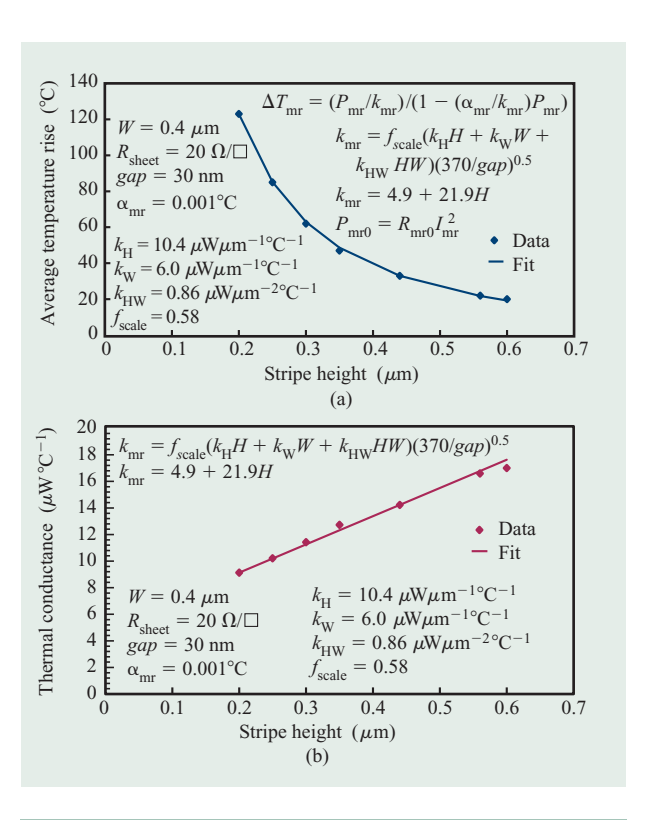


## Figure 10

Data and fit of (a) average sensor temperature rise and (b) thermal conductance as a function of of stripe height for a GMR sensor with a track width of 0.4  $\mu$ m and a gap of 30 nm. Data is reproduced from Figure 2 in [19]. Reprinted with permission from [19]; © 2001 IEEE.

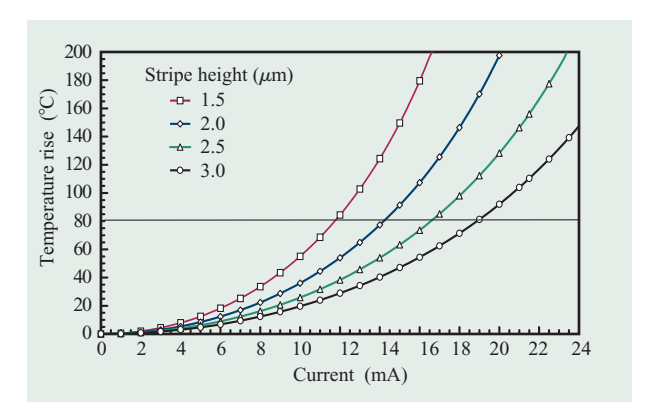
the increase in temperature with decrease in stripe height is significantly lower than would be expected by simply plotting the ratio of power densities for the two conditions, as would be predicted using a crude one-dimensional model of heat flow from a sheet resistor or assuming that the shields are at ambient temperature. Two instructive parameters are the maximum current  $(I_{\max})$  and current density  $[J_{\max}\ (=I_{\max}/H)]$  at which an AMR stripe reaches a fixed joule-heating temperature rise  $(\Delta T_{\max})$ :

$$\begin{split} J_{\text{max}} &= I_{\text{max}}/H = \sqrt{k_{\text{mr}}/HR_{\text{mr}}} \sqrt{\Delta T_{\text{max}}/(1 + \alpha_{\text{mr}}\Delta T_{\text{max}})} \\ &= \sqrt{k_{\text{mr}}/HWR_{\text{sheet}}} \sqrt{\Delta T_{\text{max}}/(1 + \alpha_{\text{mr}}\Delta T_{\text{max}})}. \end{split} \tag{9}$$

 $I_{
m max}$  and  $J_{
m max}$  are respectively plotted against stripe height in Figures 12(a) and 12(b) for a joule-heating temperature rise of 80°C for track widths of 3 and 12  $\mu$ m and gaps of 120 and 360 nm. In a simple one-dimensional heat-flow model of a thin rectangular heat source,  $k_{
m mr}$  is proportional to HW, leading to the prediction that the joule-heating temperature rise of an AMR stripe would be fixed by a constant current density that is independent of

409

<sup>&</sup>lt;sup>2</sup> Y. S. Ju, IBM Almaden Research Center, San Jose, CA, private communication (Fall 2002).



Joule-heating temperature rise as a function of current and a range of stripe heights for an AMR sensor.  $R_{\rm sheet}$  is 6.16  $\Omega/\Box$ , W is 13  $\mu$ m, and the gap is 0.37  $\mu$ m.

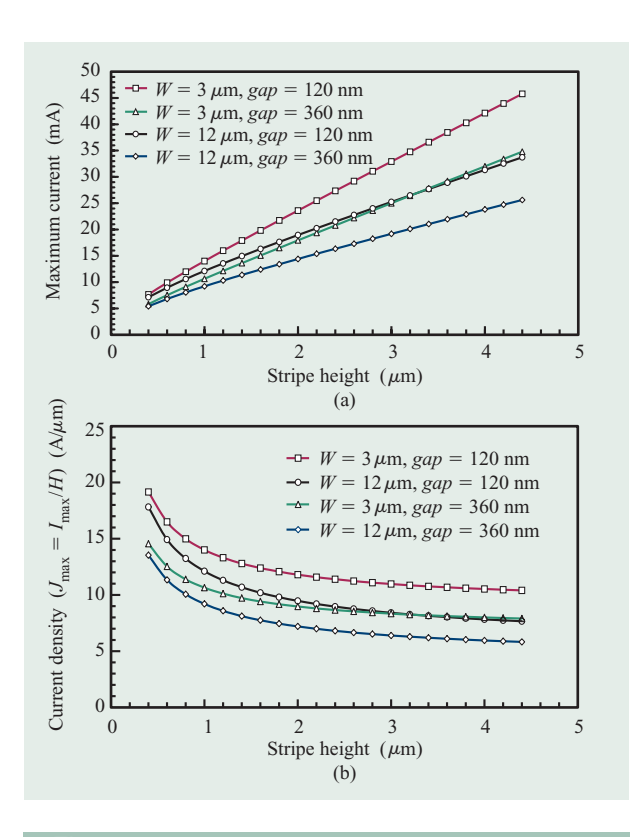


## Figure 12

Maximum current  $(I_{\max})$  (a) and current density  $(J_{\max} = I_{\max}/H)$  (b) as a function of stripe height for a joule-heating temperature rise of 80°C for a sensor with an  $R_{\rm sheet}$  of 6.16  $\Omega/\Box$  and an  $\alpha_{\rm mr}$  of  $0.0025^{\circ}C^{-1}$ . Note that  $I_{\max}/H$  is used rather than  $I_{\max}/Ht_{\rm mr}$  because the sensor has multiple layers with different values of resistivity, and thus different current densities.

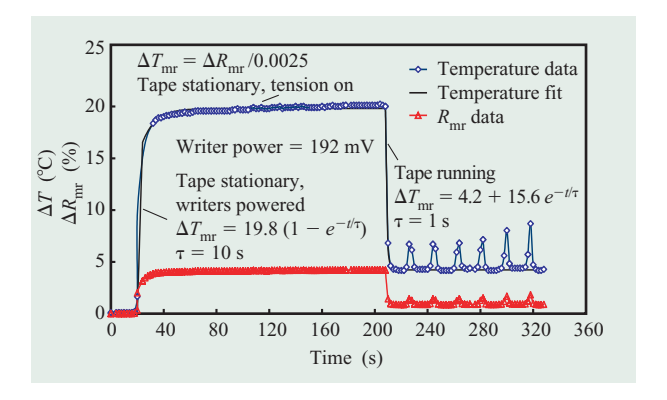


## Figure 13

Rise in resistance and temperature for an AMR sensor due to 192 mW power in the writers. The module is always in contact with the tape. At 20 s, the writers are powered. At 210 s, the tape is started moving at a speed of 3 m/s. The tape shuttles back and forth over a short section of tape, reversing directions every 18 s. The six spikes between 210 and 320 s are the AMR sensor heating while the tape is stopped during direction reversal.

either the stripe height or the track width. However, a three-dimensional heat-flow model deviates significantly from the one-dimensional model. The smaller the dimensions  $(H,\,W,\,gap)$ , the higher the current density that can be used before exceeding a fixed upper temperature limit. When  $W/H\gg 1$ , as is the case for tape heads,  $J_{\rm max}$  depends strongly on H. If W and H are comparable in magnitude, as in the case of the HDD head shown in Figure 10,  $J_{\rm max}$  has a much weaker dependence on H.

## Substrate temperature rise from writers and neighboring sensors

The data and analysis given thus far describe the selfheating of a single powered sensor. The substrate temperature will also increase above ambient in response to the heat generated by the neighboring powered sensors and writers (see Figure 1 in [24]). Figure 13 shows the rise in resistance and temperature [Equation (2)] for an unpowered sensor when seven writers are powered to a total of 192 mW. The ABS of the tape head is always in contact with the tape. In Figure 13, all writers are unpowered for the first 20 s, at which time power is applied to six writers. The temperature of the substrate rises approximately exponentially in time to a maximum increase of 19.8°C with a 1/e time constant of 10 s. At 210 s, the tape is started moving at a speed of 3 m/s with a tension of 0.6 N and an over-wrap angle of 1.5° on both the leading and trailing edges of the substrate. Following initiation of tape motion, the substrate temperature rise drops from 19.8°C to 4.2°C, with a 1/e time constant of

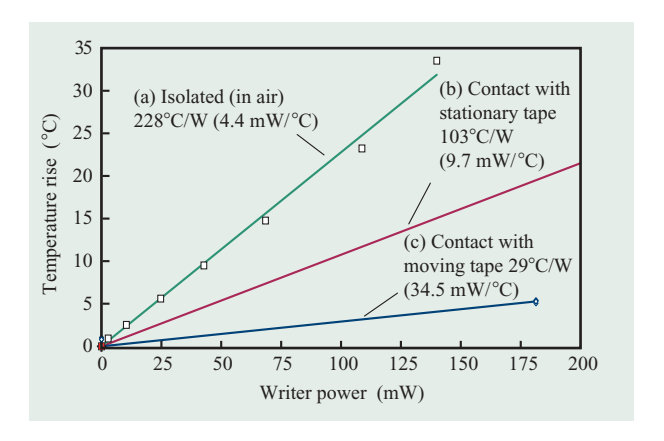
1 s. The tape is forced to shuttle back and forth across the substrate, reversing direction every 18 s. The six spikes between 210 s and 320 s are the substrate heating due to the decrease in heat dissipation associated with tape motion while the tape is stopping and reversing direction.

Figure 14 shows the substrate temperature rise plotted against writer power for the following substrate configurations: (a) isolated from the tape; (b) in contact with stationary tape; (c) in contact with tape moving at 3 m/s. The temperature rise  $(\Delta T_{\rm sub})$  of the unpowered sensor is measured to be proportional to the total power deposited into the substrate and represents an increase in the substrate temperature, as shown in Figure 13 and represented mathematically in Equation (10),

$$\Delta T_{\text{sub}} = (N_{\text{mr}} P_{\text{mr}} + N_{\text{wr}} P_{\text{wr}}) / k_{\text{sub}}, \qquad (10)$$

where  $N_{\rm mr}$  and  $N_{\rm wr}$  are respectively the number of MR sensors and writers,  $P_{\rm mr}$  and  $P_{\rm wr}$  are the power deposited into the substrate from individual sensors and writers, and  $k_{\text{sub}}$  represents the thermal leakage from the head, which is dependent on tape velocity. For an isolated substrate,  $k_{\mathrm{sub}}$ is 4.4 mW °C<sup>-1</sup> and is a combination of leakage through the cable leads and the body with which the head is in contact in a drive. Without air flow from an external source or in the absence of tape motion, the heat flux out of the substrate from conduction through the air is minimal. When the substrate is in contact with the tape, an additional leakage is introduced as a result of the thermal conduction of heat to the tape surface, for a  $k_{\text{sub}}$  of 9.7 mW °C<sup>-1</sup>. When the tape is moving at 3 m/s,  $k_{\text{sub}}$  is 34.5 mW °C<sup>-1</sup> an increase of 24.8 mW  $^{\circ}\text{C}^{-1}$  resulting from the motion of the tape. Experimentally, the temperature rise of a powered reader above the local substrate temperature is not substantially affected by the presence or lack of heat dissipation or by tape motion across the head ABS. Thus, the self-heating temperature rise of a sensor above the substrate is still given by Equation (3). The temperature of an AMR sensor, then, is given by the ambient drive temperature plus the self-heating temperature rise plus the substrate joule-heating temperature rise, as quantified in Equations (3) and (10), respectively.

The flow of heat from the substrate to the tape can be understood with a heat-flow analysis in which heat flows from the head substrate to the moving magnetic iron-oxide particulates on the tape surface. The particulates heat up as they flow, eventually approaching the temperature of the substrate if the contact time is of a sufficient duration. For the flat-contoured tape heads of this study, when the tape passes over the leading edge of the ABS, air is *skived* off (or moved) to the extent that the pressure is  $\sim 0.9$  atm and  $\lambda$ , the mean free path of the air ( $\sim 109$  nm at 300K and 0.9 atm), is significantly larger than d, the substrate–tape spacing ( $\sim 30$  nm). Because  $2 \ll d$ , subcontinuum behavior must be taken



#### Figure 14

AMR temperature rise for an unpowered sensor as a function of power deposited into the substrate from writers: (a) Isolated head; (b) Head with heat sink, but tape stationary; (c) Head with heat sink, tape moving at 3 m/s.

into account, and the thermal conductance per unit area,  $F_{\rm sp}$ , for heat flow from the substrate to an iron-oxide particulate on the tape surface is given [19] by

$$F_{\rm sp} = k_{\rm air} / \left[ d + \lambda \left( \frac{2 - \alpha_{\rm T}}{\alpha_{\rm T}} \right) \left( \frac{4\gamma}{\gamma + 1} \right) / P_{\rm r} \right], \tag{11}$$

where the thermal accommodation number  $\alpha_{\scriptscriptstyle T}$  may be taken as 1, the Prandtl number  $P_r$  may be taken as 0.7, and the specific heat ratio  $\gamma$  for diatomic molecules is 7/5. The thermal conductivity  $k_{air}$  of air is 0.026 W m<sup>-1</sup> °C<sup>-1</sup> and is a weak function of pressure, while  $\lambda$  varies approximately as the inverse of the air pressure [25]. The subcontinuum model, then, results in a thermal conductance of  $7.6 \times 10^4 \text{ W m}^{-2} \,^{\circ}\text{C}^{-1}$ , which is only 8% of the value determined using only the substrate-tape spacing (d) shown in the denominator of Equation (11). The heated substrate area is approximately the product of the width spanned by the line of heated writers (L) and the distance that heat diffuses perpendicular to the line of writers (s), which is aligned with the direction of tape motion. In this experiment, L is about 2 mm, and s is roughly in the range 0.3-0.6 mm. For stationary tape, using the flux calculated by Equation (11) and a hot ABS area of 1 mm<sup>2</sup> yields a thermal conductance of 76 mW °C<sup>-1</sup>, which is 17 times the experimental value of 4.5 mW °C<sup>-1</sup>. Matching the calculated and experimental thermal conductance values requires that the tape surface temperature be only 1.2°C cooler than the substrate temperature, rather than at ambient temperature.

The increased thermal conductance measured when the tape is moving can be accounted for by using a dynamic heat-transfer model. As a section of the tape surface first

passes under the hot region of the substrate ABS, it is at ambient temperature, and a maximum heat transfer is achieved. As the tape section travels along under the hot region of the substrate ABS, it heats up, thereby decreasing the heat transfer with distance. The heat transfer with distance along the substrate in the direction of tape motion decreases as the temperature differential between the substrate  $(T_{\rm sub})$  and the tape surface  $(T_{\rm tape})$ approaches its equilibrium value. Equation (12a) is a simplified equation describing heat flow from the substrate to the tape surface, where the equilibrium temperature of the tape surface is taken to be the substrate temperature, and the thermal conductances resulting from the thermal gradients along the plane of the tape and from the cable leads and other heat sinks are lumped into the zero velocity thermal conductance:

$$dT_{\rm tape}/dt = -(F_{\rm sp}/C_{\rm v}h)(T_{\rm tape} - T_{\rm sub}) = (1/\tau)(T_{\rm tape} - T_{\rm sub}); \eqno(12a)$$

$$T_{\text{tane}}(t) = T_{\text{sub}}(1 - e^{-t/\tau}).$$
 (12b)

 $C_{v}$  is the effective volumetric heat capacity and is equal to the product of the density  $\rho$  and heat capacity  $C_{\rm p}$ , and the quantity  $\tau$  is given by  $F_{\rm sp}/C_{\rm v}h$ . The quantity  $C_{\rm v}$  is about  $1.7 \times 10^6$  J m<sup>-3</sup> °C<sup>-1</sup> for the magnetic coating, the underlayer, and the PEN layer. The term h is the maximum penetration depth of heat into the tape for the time during which the tape is beneath the hot section of the head. To determine the depth of penetration h through a medium with a thermal conductivity of  $k_{\text{tape}}$  within the time  $t_{\text{d}}$ , one can use the approximate relationship  $k_{\text{tape}}/C_{\text{v}} \sim h^2/t_{\text{d}}$ . Given a thermal conductivity of 0.41 W m<sup>-1</sup> °C<sup>-1</sup> for the top layers and a thickness of 2.2 µm, heat will penetrate through the top layers within about 20 µs, or 20% of the 100-µs time for the tape to flow past a 300-µm hot section of the head. Thus, within 100  $\mu$ s, heat will penetrate the top layers and into the PEN layer, whose thermal conductivity is about half that of the top layers. If the tape is treated as being homogenous, with a value for  $k_{\text{tabe}}$  of 0.3 W m<sup>-1</sup> °C<sup>-1</sup>, which is intermediate between the different layers, heat will penetrate  $\sim 4.2 \ \mu m$  into the tape within 100  $\mu s$ . Using 4.2  $\mu$ m for h then yields a value for  $\tau$  of 89  $\mu$ s. Because the heat flux decreases with the decrease in temperature differential between the substrate and the tape surface, the substrate thermal conductance  $(k_{sub})$  will be decreased from its value calculated with a heat sink fixed at the ambient temperature,

$$k_{\text{sub}} = (F_{\text{sp}}L/T_{\text{s}}) \int_{0}^{s} dx (T_{\text{s}} - T_{\text{p}})$$
$$= F_{\text{sp}}Lv\tau \int_{0}^{slv} dt e^{-t/\tau}$$

$$= F_{\rm sp} L v \tau (1 - e^{-slv\tau})$$

$$= C_{\rm v} L h v (1 - e^{-slv\tau}), \tag{13}$$

where v is the velocity of the moving tape. With increasing  $s/v\tau$ , the thermal conductance approaches an asymptotic value of  $F_{\rm sp}Lv\tau$  (=  $C_{\rm v}Lhv$ ), which is 42.8 mW/°C using the parameters given above and a tape speed of 3 m/s. For s of 0.3  $\mu$ m,  $s/v\tau$  is 1.8 and  $k_{sub}$  is 27.5 mW/°C, which is within the accuracy of the experimental value of 25.8 mW/°C. A one-dimensional heat-flow analysis through the thickness of the tape using the thermal properties and dimensions given in the materials section, a tape speed of 3 m/s, and an s of 0.3  $\mu$ m yields a thermal conductance equal to the experimental value, indicating that the simple model presented above is sufficient, given the uncertainties in the parameters. A more accurate analysis of the heat transfer would include the thermal conductivities of the tape materials with the complete thermal diffusion equations, a FEA of the thermal distribution along the ABS, and experimental data over a range of velocities. The analysis given above, though, yields a simple approximate picture of the problem.

## **Summary and conclusions**

The experimental data shows that the measured thermal conductance of a shielded rectangular-sheet AMR sensor is an excellent parameter to use for analyzing the average sensor temperature or for concisely quantifying experimental or FEA data. The thermal conductance of a shielded rectangular-sheet conductor can be fit to a second-order equation in stripe height and track width with an inverse dependence on the square root of the gap thickness. The sensor thermal conductance is strongly dependent on the gap thickness because the shields are the major source of heat flow away from the sensor. Materials properties such as thermal conductivity are contained within the thermal conductance parameters. Measuring the thermal conductance over a range of geometries and adjusting the thermal conductivities used in the FEA results in a better determination of the material thermal conductivities used in the product than can be achieved with a single geometry.

In this paper, it has been shown that a simple phenomenological analytical model can be used both for tape and for disk heads whose dimensions range over an order of magnitude. A major observation is the fact that for a fixed upper limit of the sensor temperature, the smaller the dimensions, the higher the current density that can be used before exceeding a fixed upper temperature limit. The reason for the temperature rise not being constant for constant current density is the three-dimensional nature of heat flow; it results from the fact

that the linear terms  $(k_{\rm H}H \ {\rm and} \ k_{\rm W}W)$  are dominant for the long-range heat flow away from the sensor rather than the quadratic term  $(k_{\rm HW}HW)$ . One consequence of smaller sensors being able to sustain higher current densities for a fixed temperature rise is that an electromigration phenomenon, which might not be present in thicker sensors, could become a dominant reliability issue with smaller dimensions [6, 11, 12].

It has been shown that the three thermal conductance parameters are sufficient to characterize or analytically represent the thermal properties of a shielded thin-sheet resistive sensor over a wide range of geometries. These parameters can then be used to summarize either experimental or FEA data and to quantitatively compare different sensor designs. A design engineer can also use the three thermal conductance parameters to analytically characterize the temperature of the sensor operating at different current levels for a range of geometries, and to extrapolate to next-generation devices. However, an experimental approach and FEA are still necessary to accurately determine the thermal conductance parameters, especially because the properties of ultra-thin films can deviate substantially from their bulk values. Also, changes in shield materials will dramatically affect the thermal conductance of the readers. FEA can also be used to accurately determine the spatial distribution of temperatures, including the shield temperatures.

To determine the operation temperature of a sensor operating in a drive, besides the joule heating of the individual sensors, joule heating from the surrounding sensors and writers must also be included, as well as heat leakage as a function of tape velocity. The data show that, for tape heads, care must be taken to limit the total power into the substrate from both sensors and writers to avoid raising the temperature to values that could cause damage to the tape or create tribology issues associated with a hot stripe, shield, or substrate in contact with tape. When the tape is stationary, the temperature of the tape surface approaches that of the substrate. Moving tape continuously brings to the substrate a new section of tape surface which is at ambient drive temperature, resulting in significantly more cooling and thereby minimizing the concern for thermally induced damage to the tape.

## **Acknowledgments**

The authors thank all members of the IBM Tape Head Development Group in San Jose, California, for their contributions to fabrication of the parts and for useful discussions. Special thanks go to S. Czarnecki and I. Iben, Sr., for reading the manuscript and offering their comments.

#### References

- 1. R. P. Hunt, "A Magnetoresistive Readout Transducer," *IEEE Trans. Magn.* 7, No. 1, 150-154 (March 1971).
- J. C. Mallinson, The Foundations of Magnetic Recording, Second Edition, Academic Press, Inc., San Diego, 1987.
- H. N. Bertram, Theory of Magnetic Recording, Cambridge University Press, Cambridge, England, 1994.
- R. H. Dee and R. F. M. Thornly, "Thermal Effects in Shield MR Heads for Tape Applications," *IEEE Trans.* Magn. 27, No. 6, 4704–4706 (June 1991).
- C. H. Bajorek and A. F. Mayadas, "Reliability of Magnetoresistive Bubble Sensors," AIP Conf. Proc. 10, 212–216 (1972).
- I. E. T. Iben, "Head Reliability of AMR Sensors Based on Thermal Stress Tests," *IBM J. Res. & Dev.* 47, No. 4, 415–428 (2003, this issue).
- R. M. Bozorth and J. F. Dillinger, "Heat Treatment of Magnetic Materials in a Magnetic Field. II. Experiments with Alloys," *Physics* 6, 285–291 (1935).
- 8. R. M. Bozorth, *Ferromagnetism*, Wiley-IEEE Press, Piscataway, NJ, 1993.
- 9. J. H. Howey, "Magnetic Behavior of Nickel and Iron Films Condensed in a Vacuum upon Various Metal Backings," *Physiol. Rev.* **34**, 1440–1447 (1929).
- G. E. Moore, P. A. Turner, and K. L. Tai, "Current Density Limitations in Permalloy Magnetic Detectors," *AIP Conf. Proc.* 10, 217–221 (1972).
- 11. A. Gangulee and F. M. D'Heurle, "Electromigration and Diffusion in Ni-Fe Thin Films," *Jpn. J. Appl. Phys. Suppl.* **2,** 625–627 (1974).
- 12. H. G. Zolla, "Thermal and Electrical Reliability of Dual-Stripe MR Heads," *IEEE Trans. Magn.* **33**, No. 5, 2914–2916 (September 1997).
- R. L. Wallace, Jr., "The Reproduction of Magnetically Recorded Signals," *Bell Syst. Tech. J.* 30, 1145–1173 (October 1951).
- B. Bhushan, Tribology and Mechanics of Magnetic Storage Devices, Second Edition, Springer-Verlag, New York, 1996.
- 15. K. F. Young, "Finite Element Analysis of Planar Stress Anisotropy and Thermal Behavior in Thin Films," *IBM J. Res. & Dev.* **34**, No. 5, 706–717 (1990).
- H. Tian, C.-Y. Cheung, and P.-K. Wang, "Non-Contact Induced Thermal Disturbance of MR Head Signals," *IEEE Trans. Magn.* 33, No. 5, 3130–3132 (September 1997)
- M. R. Gibbons, F. Liu, K. Stoev, X. Shi, X. Yan, and R. Saha, "A Heating Model Including Effects on Magnetoresistance (MR) in MR and Giant MR Heads," J. Appl. Phys. 87, No. 9, 5392–5394 (2000).
- Y. Guo and K. Ju, "An Analytical Model for MR Heads," *IEEE Trans. Magn.* 33, No. 5, 2917–2929 (September 1997).
- Y. S. Ju, R. Xu, X. Wu, N. Smith, R. Fontana, W. Lee, K. Carey, M. Ho, D. Hsiao, and B. Gurney, "A Combined Experimental and Numerical Study of Temperature Rise in GMR Sensors Due to Self-Heating," *IEEE Trans. Magn.* 37, No. 4, 1701–1703 (July 2001).
- R. G. Biskeborn and J. H. Eaton, "Flat-Profile Tape Recording Head," *IEEE Trans. Magn.* 38, No. 5, 1919–1921 (September 2002).
- 21. See http://www.matweb.com/.
- R. C. Weast, Ed., CRC Handbook of Chemistry and Physics, 56th Edition, CRC Press, Boca Raton, FL, 1976, pp. D171–D173.
- Y. S. Ju and K. E. Goodson, "Process-Dependent Thermal Transport Properties of Silicon-Dioxide Films Deposited Using Low-Pressure Chemical Vapor Deposition," J. Appl. Phys. 85, No. 10, 7130–7134 (May 1999).

<sup>\*\*</sup>Trademark or registered trademark of ANSYS Inc.

- 24. E. R. Childers, W. Imaino, J. H. Eaton, G. A. Jaquette, P. V. Koeppe, and D. J. Hellman, "Six Orders of Magnitude in Linear Tape Technology: The One-Terabyte Project," *IBM J. Res. & Dev.* 47, No. 4, 471–482 (2003, this issue).
- R. C. Reid, J. M. Prausnitz, and B. E. Poling, *The Properties of Gases and Liquids*, Fourth Edition, McGraw-Hill, Inc., New York, 1987.

Received May 16, 2002; accepted for publication December 20, 2002

Icko Eric Timothy Iben IBM Tape Head Development Group, 5600 Cottle Road, San Jose, California 95193 (iben@us.ibm.com). Dr. Iben is a Senior Engineer in the Tape Head Development group. He received his B.S. degree in physics from the University of California at Berkeley in 1980 and his Ph.D. degree in physics from the University of Illinois in 1988. Prior to joining IBM, Dr. Iben worked for three years at AT&T Bell Laboratories and New York University doing biophysics research. He then worked for General Electric Research and Development in the areas of environmental remediation, medical instrumentation, and material characterization. He has been with IBM since 1997, performing reliability testing for tape heads.

Yu-Min Lee HDD Development, Hitachi Global Storage Technologies, 5600 Cottle Road, San Jose, California 95193 (yumin@us.ibm.com). Dr. Lee is an Engineer in the HDD Testing and Evaluation Development group. He received his B.S. in power mechanical engineering from Tsing-Hua University in 1993, his M.S. degree in mechanical engineering from National Taiwan University in 1995, and his Ph.D. degree in mechanical engineering from Carnegie Mellon University in 2001. He joined IBM in March 2001.

Wenchien D. Hsiao Recording Head Development, Hitachi Global Storage Technologies, 5600 Cottle Road, San Jose, California 95193 (dhsiao@us.ibm.com). Mr. Hsiao is a Senior Engineer with the IBM Disk Drive Head Development group. He has done finite element analysis on MR heads for many years.